



# MIT Open Access Articles

## *Li 2 O Solid Electrolyte Interphase: Probing Transport Properties at the Chemical Potential of Lithium*

The MIT Faculty has made this article openly available. **Please share** how this access benefits you. Your story matters.

<b>Citation</b>	Guo, Rui and Gallant, Betar M. 2020. "Li 2 O Solid Electrolyte Interphase: Probing Transport Properties at the Chemical Potential of Lithium." <i>Chemistry of Materials</i> , 32 (13).
<b>As Published</b>	10.1021/ACS.CHEMMATER.0C00333
<b>Publisher</b>	American Chemical Society (ACS)
<b>Version</b>	Author's final manuscript
<b>Citable link</b>	<a href="https://hdl.handle.net/1721.1/143494">https://hdl.handle.net/1721.1/143494</a>
<b>Terms of Use</b>	Creative Commons Attribution-Noncommercial-Share Alike
<b>Detailed Terms</b>	<a href="http://creativecommons.org/licenses/by-nc-sa/4.0/">http://creativecommons.org/licenses/by-nc-sa/4.0/</a>

# Li<sub>2</sub>O Solid Electrolyte Interphase: Probing Transport Properties at the Chemical Potential of Lithium

Rui Guo & Betar M. Gallant\*

Department of Mechanical Engineering, Massachusetts Institute of Technology, Cambridge, MA 02139, United States.

*Keywords: Solid Electrolyte Interphase (SEI), Electrochemical Impedance Spectroscopy (EIS), Lithium oxide, Lithium anode, Lithium battery*

---

**ABSTRACT:** Lithium (Li) anodes suffer numerous challenges arising from the chemically inhomogeneous nature of the native solid electrolyte interphase (SEI), which impedes smooth plating and leads to dendrite growth. In spite of much attention paid to engineering Li interfaces of late, there is still limited understanding of the desired chemical composition of an improved Li SEI. One major challenge has been a lack of empirical data on the structure-property-performance relations in individual SEI phases, and specifically those present at a metallic Li interface, where the chemical potential imposed by Li will yield different material properties than the bulk analogues typically invoked to understand SEI behavior. Herein, we report preparation of single-component SEIs of lithium oxide (Li<sub>2</sub>O) grown *ex situ* onto Li foils by controlled metal-gas reactions, generating ‘deconstructed’ model interfaces with nanoscale thickness (20–100 nm) similar to the native, yet more complex multiphasic SEI. The model Li|Li<sub>2</sub>O electrodes serve as a platform for further chemical and electrochemical characterization. In particular, electrochemical impedance spectroscopy, combined with interface modeling, is used to extract transport properties (ionic conductivity, diffusivity, charge carrier concentration and activation energy barriers) of Li|Li<sub>2</sub>O in symmetric cells with EC/DEC electrolyte. The Li<sub>2</sub>O SEI is further studied as a function of synthesis condition, revealing microstructural sensitivities that can be tuned to modulate transport behaviors. Finally, results are compared with single-phase Li|LiF interfaces synthesized herein and with the native SEI to isolate chemistry- and structure-specific differences.

---

## 1. Introduction

Li metal is an attractive material for future high-energy-density batteries because of its large gravimetric capacity (3860 mAh/g<sub>Li</sub> vs. 372 mAh/g<sub>graphite</sub>) combined with low negative electrochemical potential (-3.04 V vs. SHE), unique among candidate anode materials.<sup>1, 2</sup> However, the tendency towards dendritic growth has been a formidable issue, as dendrites not only induce capacity fade by consuming electrolyte and creating dead Li<sup>3</sup> but also lead to intolerable safety issues such as short circuits.<sup>4</sup> Following numerous studies on the mechanism of roughened Li deposition and dendrite growth,<sup>5, 6</sup> it is now generally accepted that the inhomogeneous nature of the solid electrolyte interphase (SEI)<sup>7, 8</sup> underlies these issues. The native SEI is conventionally described as having a multiphasic structure containing fully-reduced, dense ionic phases (e.g. Li<sub>2</sub>O, LiF) closest to the Li interface in the “inner layer”, and lithium carbonate (Li<sub>2</sub>CO<sub>3</sub>), less-reduced semi-carbonates and organic Li salts (e.g. CH<sub>3</sub>OCO<sub>2</sub>Li and CH<sub>3</sub>CH<sub>2</sub>OLi) comprising a porous “outer layer” closest to the electrolyte.<sup>9</sup> Although these phases are poor ionic conductors in bulk form, the nanoscale SEI thickness (tens of nm) permits Li<sup>+</sup> transport.<sup>8</sup> However, the chemically non-uniform native interface is readily compromised during Li cycling, leading to inhomogeneous deposition and breakdown of the fragile SEI.

To address these challenges, researchers have adopted two overarching approaches. The first has been to engineer improvements in Li cyclability through design of new electrolyte formulations including additives (e.g., LiNO<sub>3</sub>, fluoroethylene carbonate (FEC)) or other highly fluorinated compounds.<sup>10-13</sup>

Others conducted *ex situ* modification of Li foils, creating a so-called “artificial SEI” (e.g. LiF, Li<sub>3</sub>N, Al<sub>2</sub>O<sub>3</sub>, or MoS<sub>2</sub>) that attempts to decouple Li from the electrolyte and thus reconceive the SEI chemistry.<sup>14-18</sup> Such Li modification strategies are still in early days and the practical viability of such strategies has yet to be determined.

On the other hand, multiple studies have sought to develop improved fundamental understanding of the properties and function of individual phases within the native SEI. Efforts have focused predominantly on ionic SEI components (*i.e.* LiF, Li<sub>2</sub>O and Li<sub>2</sub>CO<sub>3</sub>) which have been studied intensively by molecular dynamics (MD) simulations, density functional theory (DFT) calculations as well as experimental conductivity measurements.<sup>19-22</sup> Chen *et al.*,<sup>19</sup> positing vacancies to be the majority carrier in the SEI, found by DFT that Li<sup>+</sup> diffusion in bulk Li<sub>2</sub>O and Li<sub>2</sub>CO<sub>3</sub> can be very fast (migration energy barriers of 0.2–0.5 eV) under these assumptions. Benitez *et al.*<sup>20</sup> found by MD simulations that the predominant diffusion mechanisms are vacancy assisted and knock-off diffusion in LiF, direct ion-exchange in Li<sub>2</sub>O and vacancy and knock-off diffusion in Li<sub>2</sub>CO<sub>3</sub>. Lorger *et al.*<sup>21</sup> also invoked vacancies as the charge carriers in bulk crystalline Li<sub>2</sub>O based on sintered pellet measurements, but found that the measured ionic conductivities did not match well with those of typical SEI layers in Li cells. Possible effects of grain boundaries have also been investigated in these phases.<sup>22, 23</sup> However, fewer studies have investigated the SEI integrated onto Li metal. Given the experimental challenges, most efforts have been computational.<sup>24-26</sup> Shi *et al.*<sup>24</sup> found that the dominant charge carriers of crystalline Li<sub>2</sub>CO<sub>3</sub> at potentials close to Li metal are not Li<sup>+</sup> vacancies, which predominate at

higher potentials, but rather interstitials, which migrate *via* a knock-off mechanism with diffusivity as high as  $D = 1.1 \times 10^{-7}$  cm<sup>2</sup>/s. Meanwhile, Yildirim *et al.*<sup>25</sup> found by DFT that the predominant charge carriers in LiF are Li<sup>+</sup> vacancies in the potential range 0–4 V vs. Li/Li<sup>+</sup>, although it was noted that a knock-off mechanism of Li<sup>+</sup> interstitials could provide a much faster migration pathway if available. Overall, while understanding of model interfaces has progressed substantially, a unified understanding of SEI function, and especially transport, has yet to emerge given varying assumptions and approaches taken to describe the Li interface.

In this context, this work seeks to provide new experimental insight into transport within the Li SEI, and specifically, into the contributions of individual ionic phases omnipresent at such interfaces with a particular emphasis on Li<sub>2</sub>O. Although Li<sub>2</sub>O has been extensively studied as a bulk material, *e.g.* as sintered pellets, single crystals or bulk powders, and characterized electrochemically in bulk by electrochemical impedance spectroscopy (EIS) or solid state nuclear magnetic resonance (NMR) measurements,<sup>21, 27–32</sup> the microstructure, ionic and chemical properties of such materials may not adequately describe those occurring in an SEI on Li, with vastly different chemical potentials. To address this issue, we herein report synthesis and characterization of all-Li<sub>2</sub>O SEIs grown directly on Li by O<sub>2</sub> gas treatment of Li foils under moderate reaction conditions (25–250 °C). The resulting interfaces are thin (20–100 nm) and conformal to Li, serving as an appropriate model to study a ‘deconstructed’ SEI with Li<sub>2</sub>O as the sole component. Ionic conductivity, charge carrier concentration, and carrier diffusivity within the Li<sub>2</sub>O interface are measured *in situ* by analyzing EIS data based on an appropriate underlying physical model of the interface.<sup>33, 34</sup> Results are also compared with similarly-formed Li|LiF interfaces synthesized using a fluorinated gas reactant.<sup>35</sup> As much as three orders-of-magnitude difference in ionic conductivity is observed between the single-component Li<sub>2</sub>O SEI ( $\sim 10^{-9}$  S/cm) and that of sintered bulk Li<sub>2</sub>O pellets reported in literature<sup>21</sup> ( $\sim 10^{-12}$  S/cm) at room temperature, underscoring the conclusion that Li-derived interphases present in actual battery environments differ significantly from their bulk counterparts.

## 2. Experimental Methods

### 2.1. Synthesis of Li<sub>2</sub>O or LiF Interfaces on Li

All handling of Li electrodes was conducted in an Ar-filled glovebox (MBraun) with O<sub>2</sub> and H<sub>2</sub>O contamination below 0.1 ppm. Li foil ( $\geq 99.9\%$ , Alfa Aesar) was mechanically polished using an electric grinder with an aluminum oxide grinding tip (Dremel), then rolled and punched to circles of 15-mm diameter. Punched foils were then loaded into a home-made stainless-steel reaction vessel (Kurt J. Lesker Co.) and purged with ultrapure O<sub>2</sub> (99.999%, Airgas, for Li<sub>2</sub>O) or NF<sub>3</sub> (99.999%, Electronic Fluorocarbons, LLC, for LiF) within the glovebox. The vessel was then pressurized to a gauge pressure of 240 kPa before being sealed and transferred to a thermal chamber held at the target reaction temperature (25–250 °C). After treatment (1–24 hours), the reaction vessel was opened under active vacuum and all gases were removed before being transferred directly back to the Ar glovebox. Note that the LiF film thickness ( $\sim 50$  nm) was slightly higher than in our previous report,<sup>35</sup> where the metal/gas reaction was conducted on a hot plate, due to slight differences in heating and thus reaction environment.

### 2.2. Electrochemical Measurements

Symmetric Li-Li cells, in which both electrodes were modified by Li<sub>2</sub>O or LiF as indicated, were assembled in 2032-type coin cells with one piece of Celgard 2325 separator (previously dried in a vacuum oven (Buchi Corp.) at 65 °C for 12 hours) and 20  $\mu$ L electrolyte (1.0 M LiPF<sub>6</sub> in EC/DEC, v/v = 1/1, used as received from Sigma-Aldrich). EIS measurements were conducted on a Biologic VMP3 system with a frequency range of 1 MHz to 10 mHz. EIS fitting was conducted using EC-Lab Zfit software and was fit over the frequency range of 20 kHz to approximately 20 Hz, the lower bound of which varied from cell-to-cell due to overlap of the secondary arc in the low-frequency region. Error bars for EIS measurements in **Fig. 3c** reflect standard deviations calculated from 3–6 cells. The sensitivity of the EIS fitting and the transport properties derived from the fitting results are summarized in the Supporting Information.

### 2.3. Film Characterization

SEM images were taken with a Zeiss Merlin SEM at an accelerating voltage of 1 kV. Samples were transferred to the SEM without exposure to air *via* a transfer vessel (Semilab Inc.) built for the Zeiss SEM airlock. Error bars for the SEM-determined thickness in **Fig. 3c** were determined from measurements at three random positions on the edges of the cross-section views in **Fig. 2d-f**. XPS analysis was conducted on a PHI VersaProbe II X-ray Photoelectron Spectrometer equipped with a floating voltage Ar single-ion gun for depth profiling. Samples were transferred to XPS with an air-sensitive transfer vessel to minimize exposure to air. Binding energies were calibrated by the adventitious carbon peak at 284.8 eV.<sup>36</sup> Ar-ion sputtering for XPS depth profiling was carried out at a beam acceleration of 2 kV and current of 2  $\mu$ A over an area of 2 mm  $\times$  2 mm. The sputtering rate calibrated separately on a SiO<sub>2</sub> surface was  $\sim 2.8$  nm/min. Error bars for XPS depth profiles in **Fig. 3c** were determined based on uncertainty in etching time intervals.

## 3. Results and Discussions

### 3.1. Characterization of the Li<sub>2</sub>O SEI Prepared by Metal-Gas Reaction

To fabricate a single-component SEI grown directly on Li, Li foils were reacted in O<sub>2</sub> gas at fixed temperature ranging from 25 °C to 250 °C for 1 hour, forming a compact layer of Li<sub>2</sub>O.<sup>37–39</sup> Air-exposure of post-reacted Li (**Fig. 1a**) indicated the protective effect of the formed Li<sub>2</sub>O surface layer. When exposed to the ambient environment with relative humidity of 10%, pristine Li tarnished immediately and blackened fully over 30 minutes. In contrast, the Li pre-treated by O<sub>2</sub> showed outcomes that depended on the treatment conditions. Li foils treated at 25 °C (1 hour) exhibited similar air reactivity as pristine Li, indicative of minimal quantities of imparted Li<sub>2</sub>O; in contrast, those treated at higher temperatures showed impeded (at 100 °C) or no (at 175 or 250 °C) air reactivity, indicating formation of a Li<sub>2</sub>O interface with sufficient coverage. Li surfaces showed significant roughness after treatment at 250 °C (1 hour) that was visible by eye, which was caused by the melting and re-solidification of Li metal ( $T_m = 180.5$  °C) underneath the Li<sub>2</sub>O surface layer. Longer treatment times at lower temperatures (*e.g.*, 24 hours at 175 °C) also showed excessively thick Li<sub>2</sub>O layers ( $> 500$  nm, **Fig. S1**). Thus, all further samples utilized 1-hour reaction time for further study.

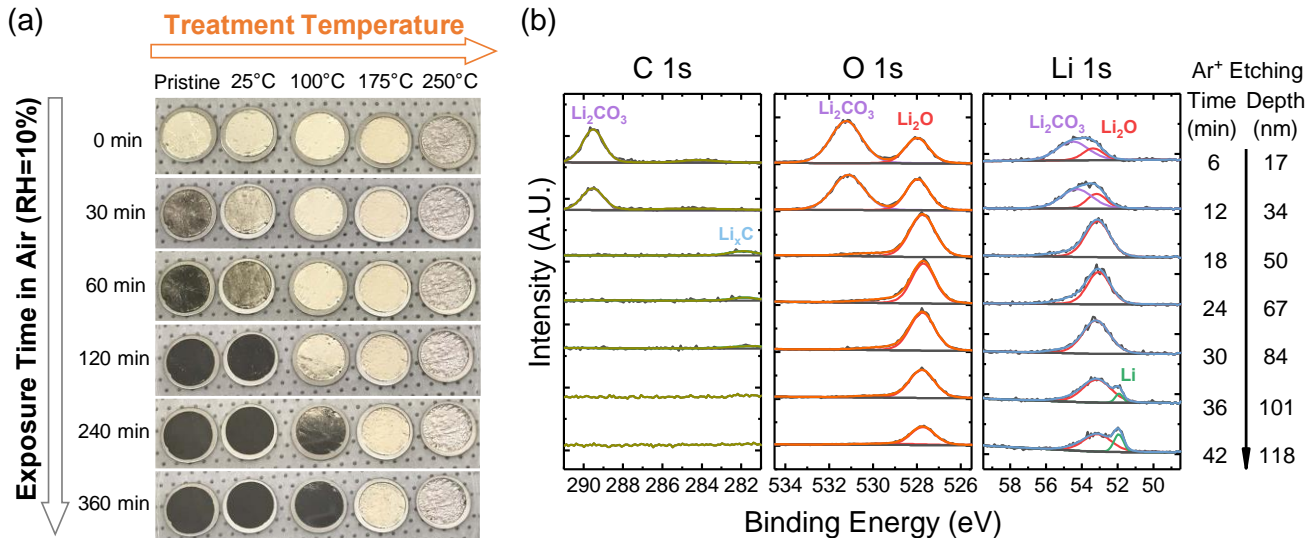


**Figure 1.** (a) Air-exposure experiment for pristine Li and for Li treated in pure O<sub>2</sub> gas for 1 hour at temperatures ranging from 25–250 °C. (RH = relative humidity = 10%). (b) XPS depth profile of Li|Li<sub>2</sub>O samples formed at 250 °C for 1 hour.

XPS depth profiling by Ar-ion etching (**Fig. 1b**) confirmed that the major component of the surface of treated Li (O<sub>2</sub>, 250 °C for 1 hour) was Li<sub>2</sub>O. The etching rate was calibrated separately to be ~2.8 nm/min using a 50-nm thick SiO<sub>2</sub> layer on a Si wafer. Some quantities of Li<sub>2</sub>CO<sub>3</sub>, as indicated by peaks in the O 1s (531.4 eV) and C 1s (289.8 eV) spectra,<sup>40</sup> were observed in the outer-most layers but were removed after 12 minutes of Ar-ion sputtering, and are attributable to trace contamination during sample transfer as they were not found within the bulk of the film. The remaining O 1s peak at 528.0 eV and Li 1s peak at 53.3 eV indicated the presence of Li<sub>2</sub>O throughout the layer.<sup>40</sup> Following top-surface removal, the C 1s peak was negligible, showing only minor amounts of lithium carbide species (282.2 eV)<sup>9</sup> due to reaction with trace C formed during etching. After 36 minutes, the metallic Li<sup>0</sup> peak emerged at 52.1 eV,<sup>40</sup> from which the Li<sub>2</sub>O thickness was determined: 25–30 nm for reactions between 25–175 °C, and ~100 nm at 250 °C. Similar XPS depth profiles were observed for other reaction conditions (**Fig. S2**).

Top-view SEM images (**Fig. 2a-c**) indicated that the Li<sub>2</sub>O SEI surface was smooth and conformal when formed below the melting point of Li metal. However, in agreement with optical images (**Fig. 1a**), significant roughening occurred at higher temperature (250 °C, **Fig. 2c**). Regardless, no cracks at micrometer-scale were identified. Meanwhile, tilted cross-sectional SEM images (**Fig. 2d-f**) showed the presence of the imparted Li<sub>2</sub>O layers as a function of reaction temperature (thickness measurements were made by intentionally breaking the sample to expose underlying Li). For samples treated at 100 °C and 175 °C, Li<sub>2</sub>O films were visually estimated to be 26 ± 8 and 30 ± 8 nm from **Fig. 2d** and **Fig. 2e**, respectively. A thicker Li<sub>2</sub>O film, 90 ± 25 nm, was observed for Li treated at 250 °C (**Fig. 2f**). Excellent agreement was found between SEM-determined thicknesses and those estimated from XPS depth profiles. Therefore, the modified interfaces – conformal, single-phase, with reasonable thickness (tens of nm) on the scale of the native

SEI – are appropriate to serve as model Li|Li<sub>2</sub>O interfaces for subsequent characterization.

EIS experiments were carried out in symmetric coin cells consisting of two pre-treated Li|Li<sub>2</sub>O electrodes over the first 24 hours post-cell assembly (**Fig. 2g-i**). The electrolyte was a conventional carbonate electrolyte, 1 M LiPF<sub>6</sub> EC/DEC (v/v=1/1). For all synthesis temperatures, the impedance spectra of Li|Li<sub>2</sub>O cells exhibited two distinct semi-circles. The semi-circle comprising the high-frequency range (100 kHz to 20 Hz) is typically attributed to charge transfer through the denser, inner (ionic) layer of the SEI,<sup>41, 42</sup> while a semi-circle comprising the lower frequency range (10 Hz to 10 mHz) has been attributed to the porous outer layer comprising the interface between SEI and electrolyte<sup>43, 44</sup> (EIS of untreated Li with a native SEI is included for comparison in **Fig. S3**). Although the presence of an outer layer on the Li<sub>2</sub>O SEI was initially unexpected, a recent study by Kamphaus *et al.*<sup>26</sup> utilized AIMD simulations to model the SEI-electrolyte interface, and found that the electrolyte could decompose or react with an Li<sub>2</sub>O SEI layer. In addition, Aurbach *et al.*<sup>45</sup> suggested that Li<sub>2</sub>O can be nucleophilic towards carbonate electrolyte. Thus, we postulate that the second semi-circle observed herein can be explained by reaction of the outer-most interface of Li<sub>2</sub>O with electrolyte upon soaking, creating a distinct outer layer, likely porous, in addition to the Li<sub>2</sub>O inner layer. The Li<sub>2</sub>O SEI prepared at 100 °C showed relatively stable impedance over the first 12 hours following cell assembly (**Fig. 2g**), with a small increase in both high- and low-frequency arcs after 24 hours, indicating that Li was not fully protected by Li<sub>2</sub>O in agreement with the air-exposure experiments. In contrast, the Li<sub>2</sub>O SEI formed at 175 °C was more stable over 24 hours, with slight changes in the low-frequency region between 0–12 hours (**Fig. 2h**), possibly due to as-described reactions at the outer SEI/electrolyte interface. The EIS results of Li<sub>2</sub>O formed at 250 °C exhibited the largest variations during resting (**Fig. 2i**), suggesting higher reactivity at the interface of SEI and electrolyte due to its rougher surface morphology.

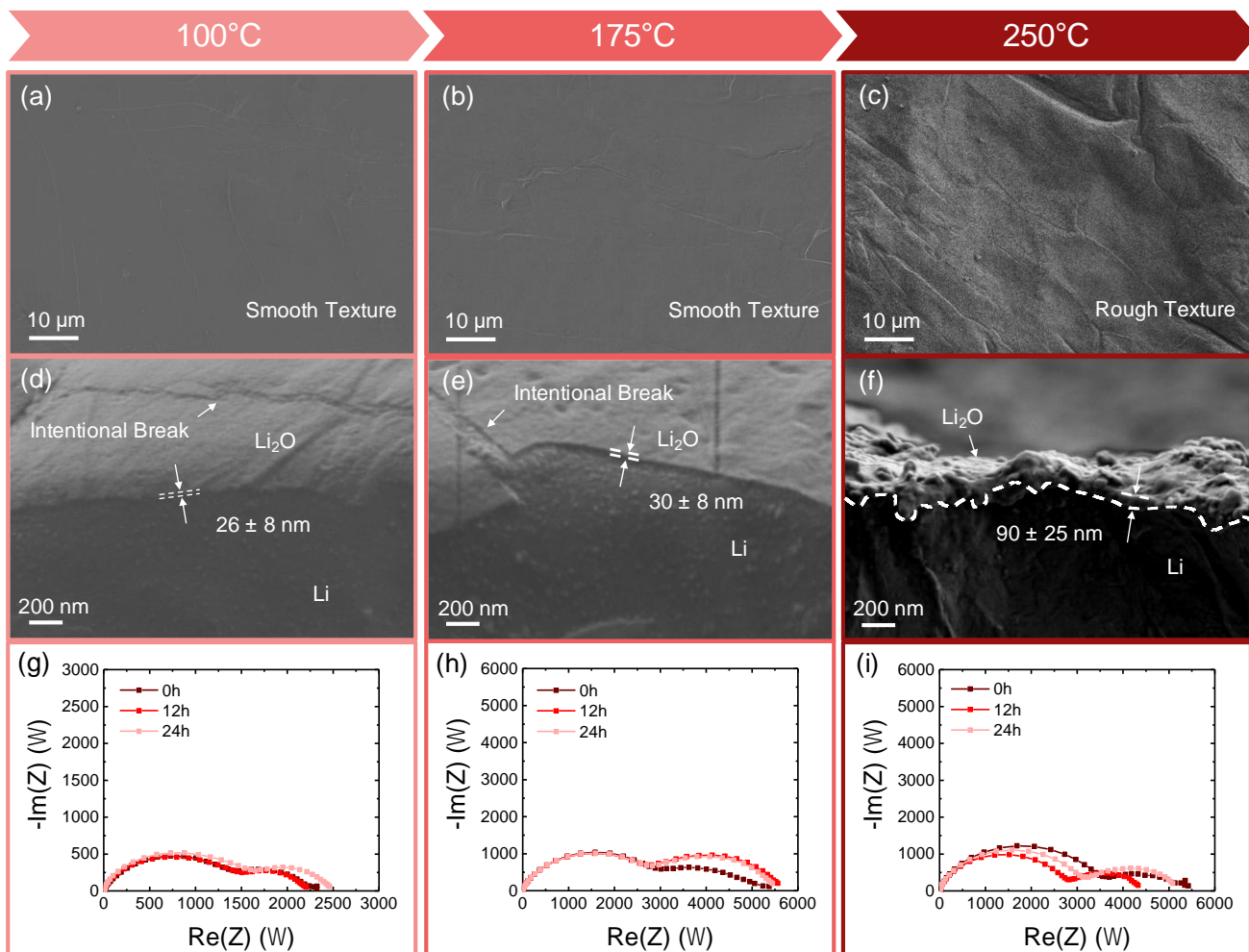


**Figure 2.** (a-c) Top view and (d-f) cross-section view of SEM images of Li|Li<sub>2</sub>O prepared at (a, d) 100 °C, (b, e) 175 °C and (c, f) 250 °C for 1 hour. (g-i) Nyquist plots of symmetric coin cells of Li|Li<sub>2</sub>O prepared at (g) 100 °C, (h) 175 °C and (i) 250 °C for 1 hour. The electrolyte was 1 M LiPF<sub>6</sub> EC/DEC (v/v=1/1).

### 3.2. Equivalent Circuit and Physical Model of SEI

Previously, Aurbach et al.<sup>44</sup> proposed a circuit model consisting of five series RC circuits to describe the multilayer nature of the native SEI in both carbonate- and ether-based electrolytes, where five was the minimum number necessary to achieve adequate fitting. Peled et al.<sup>23</sup> further considered contributions of grain boundaries of each sublayer to overall SEI impedance, which necessitated cautious examination of the physical meaning of each RC circuit in the SEI model. Given different proposed models in literature, Churikov et al.<sup>33, 34</sup> compared multiple equivalent circuit options, and developed a relatively simple model for the charge transfer process of the SEI based on empirical analysis. The proposed model consisted of only one bulk SEI layer with a space-charge region at the metal/SEI interface, and also accounted for the diffusion of ionic charge carriers in the vicinity of the space-charge region. The results could attain an excellent fit to the EIS data using an equivalent circuit containing only four elements (vs. 10–15 in previous models), helping to avoid potentially ambiguous fitting results, over-fitting, or uncertain physical meanings.

We adopted this model to describe the physical behavior and transport within the solid-state Li<sub>2</sub>O interface on Li, and specifically, within the higher-frequency arc corresponding to the

compact inner layer. A schematic of the SEI model and corresponding equivalent circuit are shown in **Fig. 3a**. Given the differences in chemical potentials (Fermi levels) of Li and Li<sub>2</sub>O, a space-charge region forms at their junction due to mutual diffusion of charge carriers required to align interfacial energy levels.<sup>26, 34</sup> This space-charge layer can be modeled as having a distinct differential capacitance,  $C_{SC}$ , and a thickness characterized by the Debye length,  $L_D$ , provided that the Debye length is much smaller than the total Li<sub>2</sub>O thickness, which was verified in the following modeling results and listed in **Table S1**. Three additional elements are included to describe transport through the Li<sub>2</sub>O layer: (i) A geometric capacitance of the Li<sub>2</sub>O SEI,  $C_{SEI}$ ; (ii) An ionic resistance,  $R_{SEI}$ ; and (iii) A Warburg element,  $Z_W$ , included to capture solid-state diffusion of charge carriers in the vicinity of the space-charge region. Therefore, the equivalent circuit of a symmetric coin cell is composed of one electrolyte resistance and two identical SEI circuits in series (**Fig. S4**), further simplified into **Fig. S5** for the purpose of data fitting. To accurately capture the intrinsic behavior of Li<sub>2</sub>O, the fitting was performed in the high-mid frequency range (20 kHz to 20 Hz) but omitted the low-frequency semi-circle related to the porous outer-layer as described above. The corresponding fitting results using the above model showed excellent agreement with the EIS data (**Fig. 3b, S6**).



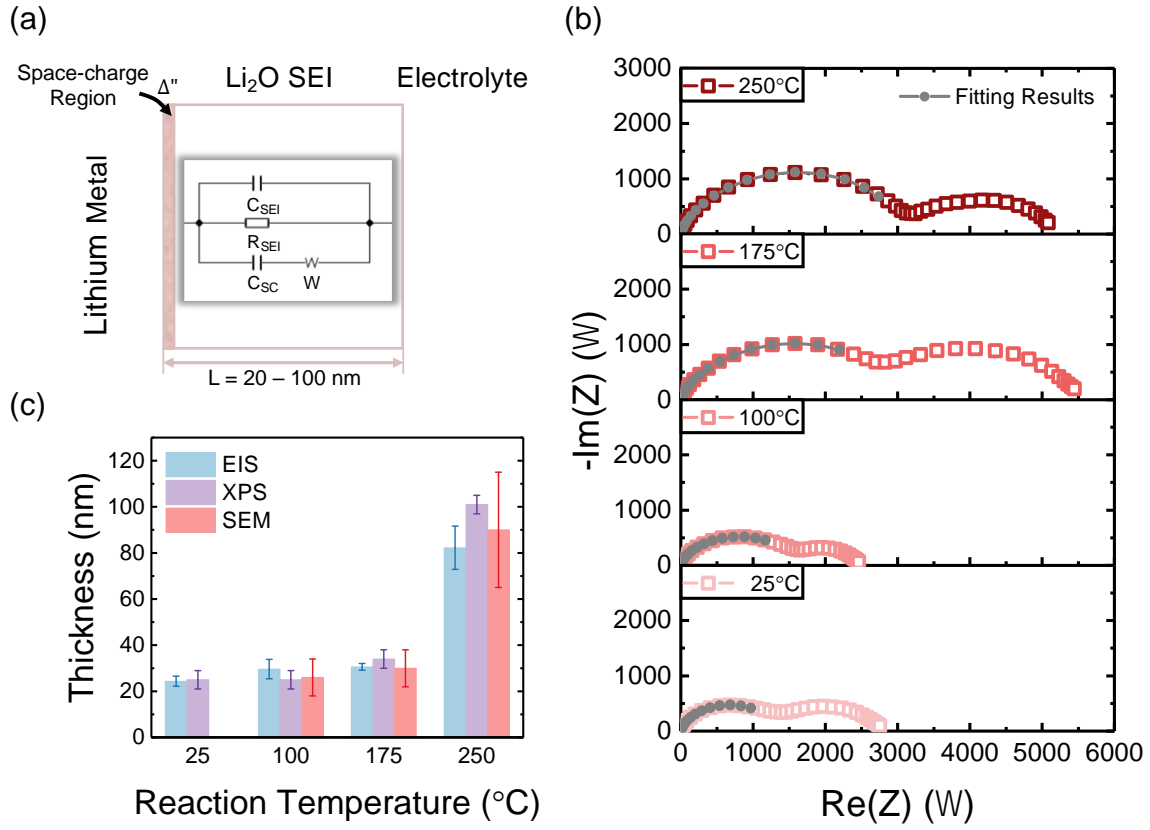


**Figure 3.** (a) SEI equivalent circuit model for a single Li| $\text{Li}_2\text{O}$  electrode (full cell equivalent circuit is shown in the Supporting Information).  $\Delta\phi$  is the potential drop across the space-charge region. (b) Nyquist plots of the EIS data and the fitting results for symmetric coin cells of Li| $\text{Li}_2\text{O}$  electrodes. (c) Summary of estimated thicknesses of the  $\text{Li}_2\text{O}$  SEI layers obtained by three different methods: SEM imaging; XPS sputtering; and as a direct output of the impedance model; error bars are described in the Experimental section. The electrolyte used in all cells is 1 M  $\text{LiPF}_6$  EC/DEC ( $v/v=1/1$ ).

Physicochemical properties of the SEI were next determined by deconstructing the expressions of the equivalent circuit elements.<sup>34</sup> With  $C_{\text{SEI}}$  and  $R_{\text{SEI}}$  acquired numerically from the fitting, the SEI thickness  $L$  and ionic conductivity  $\sigma_0$  were determined from the following expressions relevant for a planar electrode:

$$C_{\text{SEI}} = \frac{\varepsilon\varepsilon_0 A}{L} \quad (1)$$

$$R_{\text{SEI}} = \frac{L}{\sigma_0 A} \quad (2)$$

where  $\varepsilon_0$  and  $\varepsilon$  are the vacuum permittivity and the relative permittivity (dielectric constant), respectively ( $\varepsilon_{\text{Li}_2\text{O}} = 8.9$ ,  $\varepsilon_{\text{LiF}} = 9.0$ )<sup>33,46</sup> and  $A$  is the known electrode area ( $A = 1.77$  cm<sup>2</sup>). The Warburg impedance for the charge carrier diffusion is  $Z_W = \frac{\sqrt{2W}}{\sqrt{i\omega}}$ , where  $\omega$  is the angular frequency and the Warburg constant  $W$  is defined as:

$$W = \frac{k_B T}{q^2 n_0 \sqrt{2D} A} \quad (3)$$

$k_B$  is the Boltzmann constant,  $T$  is temperature,  $q$  is the elementary charge,  $n_0$  and  $D$  are the concentration and diffusivity of the charge carriers in the SEI, respectively (note that no assumptions are made as to the nature of charge carriers; see additional discussion below). The two unknowns,  $n_0$  and  $D$ , are determined by the Warburg constant in Eqn. (3) along with the Nernst-Einstein relationship for mobility,  $\mu$ :

$$\mu = \frac{\sigma_0}{qn_0} = \frac{q}{k_B T} D \quad (4)$$

Following determination of  $L$ ,  $\sigma_0$ ,  $n_0$  and  $D$ , the Debye length  $L_D$  can be therefore calculated by taking the charge carrier concentration  $n_0$  into Eqn. (5):

$$L_D = \sqrt{\frac{\varepsilon\varepsilon_0 k_B T}{2q^2 n_0}} \quad (5)$$

To validate the fitting results, the thicknesses of the SEI layers, the output of Eqn. (1), were compared with measurements of thickness mentioned previously, *i.e.* XPS depth profiles (Fig. 1b) and SEM images (Fig. 2d-f), and showed excellent agreement (Fig. 3c). Specifically, the fittings indicated an SEI thickness increasing from 20 to 30 nm for reaction temperatures increasing from 25 °C to 175 °C, and reaching 90 nm at 250 °C, highly consistent with experiments. The sensitivity of EIS measurements and fitting process to the physicochemical properties of the SEI layers are also validated in Fig. S7 and Fig. S8, respectively; conclusions were found to be highly robust to variations in assumed physical parameters ( $A$ ,  $\varepsilon$ ).

### 3.3. Measured Transport Parameters in Single-Phase SEIs

The analysis was next extended to quantify transport parameters as a function of  $\text{Li}_2\text{O}$  formation temperature. As shown in Fig. 4, below the melting point  $T_m$  of Li metal,  $\sigma_0$ ,  $D$ , and  $n_0$  remained roughly constant ( $\sim 1 \times 10^{-9}$  S/cm,  $2 \times 10^{-9}$  cm<sup>2</sup>/s, and  $2 \times 10^{-7}$  mol/cm<sup>3</sup>, respectively). However, significant changes

were observed above  $T_m$ . Specifically,  $\sigma_0$  increased by three-fold up to  $3.5 \times 10^{-9}$  S/cm;  $D$  increased from  $2.0 \times 10^{-9}$  up to  $2.8 \times 10^{-8}$  cm<sup>2</sup>/s; and  $n_0$  decreased significantly, from  $1.5 \times 10^{-7}$  mol/cm<sup>3</sup> to  $2.6 \times 10^{-8}$  mol/cm<sup>3</sup> between 175 and 250 °C. As discussed further below, the nature of charge carriers within the SEI is strongly dependent upon the chemical potential of Li;<sup>24, 25, 47, 48</sup> therefore, these changes with different reaction temperatures are more likely to reflect changes in Li<sub>2</sub>O microstructure, rather than in the fundamental nature of ion transport in the films. Compared to a native SEI (~6 to 10 nm from EIS) formed in the same carbonate electrolyte with multiple constituent phases, Li|Li<sub>2</sub>O has significantly higher  $D$  ( $1.8 \times 10^{-9}$  cm<sup>2</sup>/s vs.  $1.6 \times 10^{-11}$  cm<sup>2</sup>/s for native SEI) but lower  $n_0$  ( $1.8 \times 10^{-7}$  mol/cm<sup>3</sup> vs.  $8.5 \times 10^{-6}$  mol/cm<sup>3</sup>, respectively), resulting in an overall higher conductivity ( $\sigma_0 = 5.1 \times 10^{-10}$  S/cm for the native SEI).

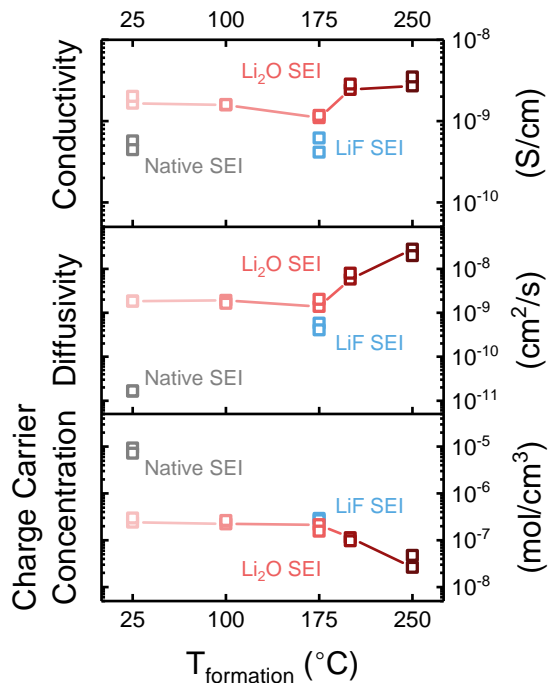


**Figure 4.** Conductivity, charge carrier diffusivity and concentration of the different SEI layers derived from the fitting results of the EIS data. Two data points are presented for each condition

Analogous studies were also conducted on an all-LiF SEI grown on Li foils using a metal-gas reaction with NF<sub>3</sub> reported previously.<sup>35</sup> The thickness of the LiF SEI formed at 175 °C was found to be ~25 nm by EIS fitting, similar to the thickness of the Li<sub>2</sub>O SEI formed at the same temperature in O<sub>2</sub> (~29 nm).  $\sigma_0$  of LiF was around  $5.2 \times 10^{-10}$  S/cm (Fig. 4), approximately half of the conductivity of Li<sub>2</sub>O and more similar to the conductivity of the native SEI.  $n_0$  of both LiF and Li<sub>2</sub>O SEI were similar. However,  $D$  in the LiF SEI (about  $4.5 \times 10^{-10}$  cm<sup>2</sup>/s) was lower than that of Li<sub>2</sub>O, which accounted for the overall lower conductivity of LiF.

Transport properties of the Li<sub>2</sub>O and LiF SEI were also investigated as a function of applied temperature in the range 9–65 °C. Fig. 5a-b and S9 show temperature-dependent EIS data of symmetric cells using either Li|Li<sub>2</sub>O or Li|LiF electrodes with interfaces formed at 175 °C for 1 hour. The resistance of the high-frequency semicircle corresponding to the ionic Li<sub>2</sub>O or LiF layer decreased significantly, up to one order of magnitude,

with increasing temperature. The resulting thickness of Li<sub>2</sub>O and LiF SEI were found, as anticipated, to be invariant with temperature (Fig. S10), whereas conductivity exhibited strong temperature-dependence (Fig. 5c). The Arrhenius plot showed a linear relationship between the reciprocal of temperature and the product of ionic conductivity and temperature in logarithmic scale, in accordance with the defect chemistry of solid-state ionic conductors.<sup>49</sup> The activation energy for conduction,  $E_a$ , was directly calculated from the slope of the Arrhenius relationship to be 0.58 eV and 0.47 eV for Li|Li<sub>2</sub>O and Li|LiF, respectively.  $D$  and  $n_0$  also showed linear relationships on Arrhenius plots for both materials (Fig. S11); diffusion energy barriers in Li<sub>2</sub>O ( $E_b = 0.49$  eV) and LiF ( $E_b = 0.35$  eV) were found to be roughly comparable to that of Li<sup>+</sup> interstitials reported elsewhere – 0.64 eV for Li<sub>2</sub>O and 0.27 eV for LiF – from computational results.<sup>25, 50</sup>

### 3.4. Discussion

The ionic conductivities of Li|Li<sub>2</sub>O obtained herein, which are derived from and tested at the chemical potential of metallic Li with electrolyte present, are significantly higher than reported literature values of bulk materials: e.g.,  $\sigma_0 \approx 10^{-12}$  S/cm for sintered pellets<sup>21</sup> as mentioned previously, in which the Li<sup>+</sup> potential within the film was estimated to be 2.8–2.9 V vs. Li/Li<sup>+</sup>.<sup>51</sup> Moreover, charge carrier diffusivities in Li|Li<sub>2</sub>O ranged from  $D = 10^{-9}$  to  $10^{-8}$  cm<sup>2</sup>/s, at least four orders of magnitude larger than that of bulk Li<sub>2</sub>O from the same pellet measurements ( $2 \times 10^{-13}$  cm<sup>2</sup>/s).<sup>21</sup> We note that our obtained conductivity values show good order-of-magnitude agreement with those of a native SEI without any interfacial modification (Fig. 4). Although experimental diffusivity values in an all-Li<sub>2</sub>O SEI have not been reported experimentally to the best of our knowledge, our obtained values agree well with those obtained from DFT calculations of Li<sub>2</sub>CO<sub>3</sub> on Li metal, with  $D$  as high as  $1.1 \times 10^{-7}$  cm<sup>2</sup>/s.<sup>24</sup> Given similar conclusions reached in studies in Li<sub>2</sub>CO<sub>3</sub> SEI,<sup>24, 47, 52</sup> it is reasonable to expect that the chemical potential of Li can promote creation of excess Li<sup>+</sup> interstitials in Li<sub>2</sub>O as well, a mechanism that is not experimentally accessible in bulk pellets. Therefore, the large differences in  $\sigma_0$  and  $D$  between Li|Li<sub>2</sub>O and sintered bulk Li<sub>2</sub>O<sup>21</sup> serve as compelling evidence that more facile Li<sup>+</sup> transport pathways may be available when Li<sub>2</sub>O is in contact with Li metal. Fig. S12 compares the Arrhenius behavior of Li|Li<sub>2</sub>O with other bulk measurements on sintered pellets measured without the presence of Li metal or electrolyte,<sup>21, 27-31</sup> emphasizing that Li|Li<sub>2</sub>O has significantly higher conductivity near room temperature.

In addition, significant changes were found in Li<sub>2</sub>O transport parameters as a function of formation temperature. We attribute this to the fact that higher reaction temperatures likely support growth of larger Li<sub>2</sub>O grain sizes and an overall decrease in grain boundary (defect) density. Although the transport pathways of Li<sup>+</sup> interstitials within the Li<sub>2</sub>O SEI (whether through grains or grain boundaries) are currently unknown, we tentatively assign this improvement in  $D$  to arise from larger grain sizes and fewer impeding grain boundaries formed at higher reaction temperatures. The decrease in  $n_0$  is also consistent with this picture: for Li<sub>2</sub>O formed at higher temperature, the Li|Li<sub>2</sub>O interface is anticipated to be more ordered with lower amounts of defects, making it more difficult to form Li<sup>+</sup> interstitials near the space-charge region. Overall, the increase in diffusivity, rather than loss of carriers, with increasing reaction temperature was more significant and dominates transport behavior, and thus the conductivity increases overall.

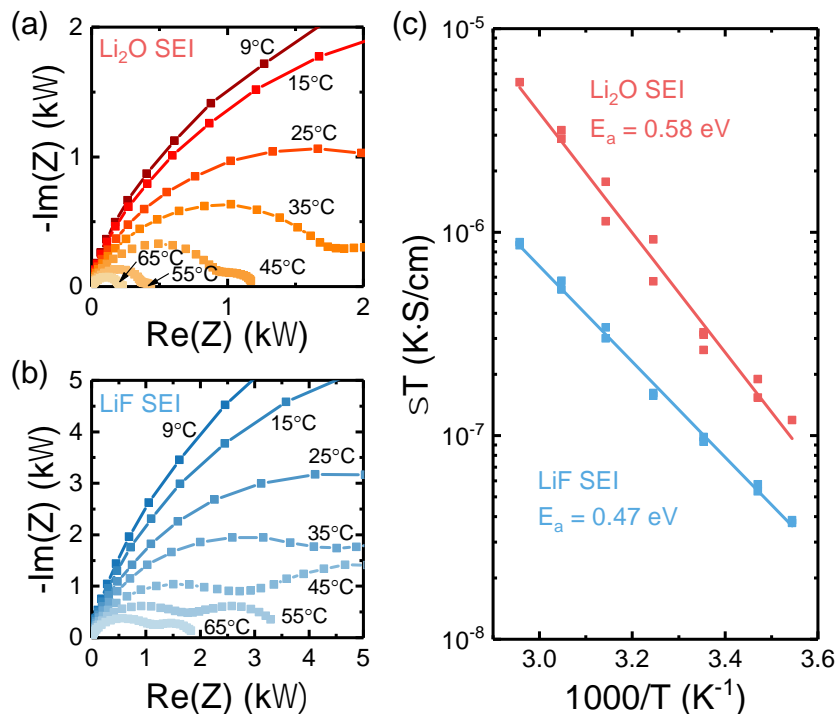


**Figure 5.** Nyquist plots of the EIS data of a symmetric coin cell using Li electrodes treated in (a)  $O_2$  at  $175^\circ C$  for 1 hour and (b) nitrogen trifluoride at  $175^\circ C$  for 1 hour. The temperature of the EIS measurements ranges from  $9^\circ C$  to  $65^\circ C$ . (c) Temperature dependence of the ionic conductivity of the  $Li_2O$  and  $LiF$  SEI. The activation energy  $E_a$  is calculated from the slope of the Arrhenius plot.

The conductivity of bulk  $LiF$  calculated elsewhere<sup>48</sup> at anodic potentials was found to be significantly lower – at approximately  $10^{-31}$  S/cm – than observed here. However,  $\sigma_0$  of  $LiF$  has been enhanced up to  $6 \times 10^{-6}$  S/cm by coating nanoscale  $LiF$  layers onto other substrates, creating highly disordered structures with ionic accumulation/depletion effects.<sup>53</sup> Therefore, it is not unreasonable to expect commensurate, relatively higher conductivity of both  $Li_2O$  and  $LiF$  when present at the metal/SEI interface with space-charge effects.

The native SEI showed over one order of magnitude higher concentration of charge carriers ( $8.5 \times 10^{-6}$  mol/cm<sup>3</sup>) than either the  $Li_2O$  or  $LiF$  SEI ( $1.8 \times 10^{-7}$  mol/cm<sup>3</sup> or  $2.7 \times 10^{-7}$  mol/cm<sup>3</sup>, respectively), reflective of its more disordered, multiphase structure. However,  $D$  of the native SEI ( $1.6 \times 10^{-11}$  cm<sup>2</sup>/s) was found to be two orders of magnitude lower than the  $Li_2O$  SEI formed at room temperature ( $1.8 \times 10^{-9}$  cm<sup>2</sup>/s). These phases in the native SEI are mostly amorphous with dispersed crystalline particles as revealed by recent cryo-TEM studies,<sup>11, 13</sup> partly because the SEI is formed by rapid reactions of Li metal and the electrolytes at room temperature under highly non-equilibrium conditions. Such highly disordered and amorphous structure of the native SEI brings about problematic migration pathways for charge carriers. A recent finding also suggests that the amorphous region in native SEI provide slower ionic transport pathways than nano-crystalline phases.<sup>54</sup> Interestingly,  $\sigma_0$  of the multiphase native SEI, at  $5.1 \times 10^{-10}$  S/cm, was lower than that of the  $Li_2O$  SEI but similar to  $LiF$  ( $\sim 5.2 \times 10^{-10}$  S/cm). We tentatively suggest that  $\sigma_0$  of the native SEI may be limited by the lower-conductivity phase,  $LiF$ , known to be omnipresent in the Li SEI due to widespread use of fluorinated salts,<sup>55, 56</sup> but the limiting compositions of the SEI will required further investigation in continued work when a larger range of model SEIs can be successfully synthesized and compared. Efforts to

systematically vary  $LiF$ -to- $Li_2O$  ratios and impart additional SEI-relevant, single-component interfaces are ongoing.

Overall, this work indicates that there is significant opportunity to obtain more precise understanding of the SEI using experimental model systems, even regarding the simplest and most common phases such as  $Li_2O$  or  $LiF$ , about which relatively little is still known in relevant battery environments. Hopefully, better quantitative understanding of the properties and functions of individual phases in the SEI can be used in the future to guide rational design of electrolytes, additives and interfaces with improved functionality for stabilizing Li interfaces.

#### 4. Conclusions

A model interface consisting of  $Li_2O$  (20–100 nm) or  $LiF$  (~25 nm) on Li was developed to obtain first measurements of transport properties of a single-phase SEI at the chemical potential of Li. Comprehensive EIS analysis indicated that the ionic conductivity and diffusivity of  $Li_2O$  on Li were several orders of magnitude higher than reported values obtained using bulk pellet measurements, which is attributable to the dramatically different chemical, ionic, and microstructural environments in a real SEI. The experimental values obtained with  $Li_2O$  and  $LiF$  are significantly closer to those of a native SEI and agree well with computational results. In addition, it was found that  $Li|Li_2O$  prepared herein has moderately higher conductivity than  $Li|LiF$ . Although the correspondence of our single-phase results with that of the native SEI requires continued testing in future work to elucidate in full, these results suggest that  $LiF$  may limit transport within the SEI, and therefore that an  $Li_2O$ -rich SEI may be equally or more functional than one enriched with  $LiF$ . Overall, this work demonstrates one path forward to increase fundamental understanding of the SEI on Li through



development of appropriate analogue interfaces that can be more-readily isolated and studied than native interfaces, and which we hope will contribute to rationalization and improvement of the SEI in future work.

## ASSOCIATED CONTENT

### Supporting Information

The Supporting Information is available free of charge on the ACS Publications website.

Additional figures and tables supporting the experiments, equivalent circuit model and EIS fitting (PDF)

## AUTHOR INFORMATION

### Corresponding Author

\*E-mail: bgallant@mit.edu

### Notes

The authors declare no competing financial interest.

## ACKNOWLEDGMENT

The authors gratefully acknowledge support from National Science Foundation under award number 1804247. This work made use of the MRSEC Shared Experimental Facilities at MIT, supported by the National Science Foundation under award number DMR-1419807.

## REFERENCES

- (1) Lin, D. C.; Liu, Y. Y.; Cui, Y., Reviving the Lithium Metal Anode for High-Energy Batteries. *Nat. Nanotechnol.* **2017**, 12, (3), 194-206.
- (2) Cheng, X. B.; Zhang, R.; Zhao, C. Z.; Zhang, Q., Toward Safe Lithium Metal Anode in Rechargeable Batteries: A Review. *Chem. Rev.* **2017**, 117, (15), 10403-10473.
- (3) Fang, C.; Li, J.; Zhang, M.; Zhang, Y.; Yang, F.; Lee, J. Z.; Lee, M.-H.; Alvarado, J.; Schroeder, M. A.; Yang, Y.; Lu, B.; Williams, N.; Ceja, M.; Yang, L.; Cai, M.; Gu, J.; Xu, K.; Wang, X.; Meng, Y. S., Quantifying Inactive Lithium in Lithium Metal Batteries. *Nature* **2019**, 572, (7770), 511-515.
- (4) Aurbach, D.; Zinigrad, E.; Cohen, Y.; Teller, H., A Short Review of Failure Mechanisms of Lithium Metal and Lithiated Graphite Anodes in Liquid Electrolyte Solutions. *Solid State Ion.* **2002**, 148, (3-4), 405-416.
- (5) Wood, K. N.; Kazyak, E.; Chadwick, A. F.; Chen, K. H.; Zhang, J. G.; Thornton, K.; Dasgupta, N. P., Dendrites and Pits: Untangling the Complex Behavior of Lithium Metal Anodes through Operando Video Microscopy. *ACS Cent. Sci.* **2016**, 2, (11), 790-801.
- (6) Shi, F. F.; Pei, A.; Vailionis, A.; Xie, J.; Liu, B. F.; Zhao, J.; Gong, Y. J.; Cui, Y., Strong Texturing of Lithium Metal in Batteries. *Proc. Natl. Acad. Sci. U.S.A.* **2017**, 114, (46), 12138-12143.
- (7) Tikekar, M. D.; Choudhury, S.; Tu, Z. Y.; Archer, L. A., Design Principles for Electrolytes and Interfaces for Stable Lithium-Metal Batteries. *Nat. Energy* **2016**, 1, 1-7.
- (8) Peled, E.; Menkin, S., Review-SEI: Past, Present and Future. *J. Electrochem. Soc.* **2017**, 164, (7), A1703-A1719.
- (9) Schechter, A.; Aurbach, D.; Cohen, H., X-Ray Photoelectron Spectroscopy Study of Surface Films Formed on Li Electrodes Freshly Prepared in Alkyl Carbonate Solutions. *Langmuir* **1999**, 15, (9), 3334-3342.
- (10) Suo, L. M.; Xue, W. J.; Gobet, M.; Greenbaum, S. G.; Wang, C.; Chen, Y. M.; Yang, W. L.; Li, Y. X.; Li, J., Fluorine-Donating Electrolytes Enable Highly Reversible 5-V-Class Li Metal Batteries. *Proc. Natl. Acad. Sci. U.S.A.* **2018**, 115, (6), 1156-1161.
- (11) Liu, Y.; Lin, D.; Li, Y.; Chen, G.; Pei, A.; Nix, O.; Li, Y.; Cui, Y., Solubility-Mediated Sustained Release Enabling Nitrate Additive in Carbonate Electrolytes for Stable Lithium Metal Anode. *Nat. Commun.* **2018**, 9, (1), 3656.
- (12) Genovese, M.; Louli, A. J.; Weber, R.; Sanderson, R. J.; Johnson, M. B.; Dahn, J. R., Combinatorial Methods for Improving Lithium Metal Cycling Efficiency. *J. Electrochem. Soc.* **2018**, 165, (13), A3000-A3013.
- (13) Li, Y. Z.; Li, Y. B.; Pei, A. L.; Yan, K.; Sun, Y. M.; Wu, C. L.; Joubert, L. M.; Chin, R.; Koh, A. L.; Yu, Y.; Perrino, J.; Butz, B.; Chu, S.; Cui, Y., Atomic Structure of Sensitive Battery Materials and Interfaces Revealed by Cryo-Electron Microscopy. *Science* **2017**, 358, (6362), 506-510.
- (14) Li, Y.; Sun, Y.; Pei, A.; Chen, K.; Vailionis, A.; Li, Y.; Zheng, G.; Sun, J.; Cui, Y., Robust Pinhole-Free Li<sub>3</sub>N Solid Electrolyte Grown from Molten Lithium. *ACS Cent. Sci.* **2018**, 4, (1), 97-104.
- (15) Cha, E.; Patel, M. D.; Park, J.; Hwang, J.; Prasad, V.; Cho, K.; Choi, W., 2D MoS<sub>2</sub> as an Efficient Protective Layer for Lithium Metal Anodes in High-Performance Li-S Batteries. *Nat. Nanotechnol.* **2018**, 13, (4), 337-344.
- (16) Zhao, J.; Liao, L.; Shi, F. F.; Lei, T.; Chen, G. X.; Pei, A.; Sun, J.; Yan, K.; Zhou, G. M.; Xie, J.; Liu, C.; Li, Y. Z.; Liang, Z.; Bao, Z. N.; Cui, Y., Surface Fluorination of Reactive Battery Anode Materials for Enhanced Stability. *J. Am. Chem. Soc.* **2017**, 139, (33), 11550-11558.
- (17) Kozen, A. C.; Lin, C. F.; Pearse, A. J.; Schroeder, M. A.; Han, X. G.; Hu, L. B.; Lee, S. B.; Rubloff, G. W.; Noked, M., Next-Generation Lithium Metal Anode Engineering via Atomic Layer Deposition. *ACS Nano* **2015**, 9, (6), 5884-5892.
- (18) Chen, L.; Chen, K. S.; Chen, X. J.; Ramirez, G.; Huang, Z. N.; Geise, N. R.; Steinruck, H. G.; Fisher, B. L.; Shahbazian-Yassar, R.; Toney, M. F.; Hersam, M. C.; Elam, J. W., Novel ALD Chemistry Enabled Low-Temperature Synthesis of Lithium Fluoride Coatings for Durable Lithium Anodes. *ACS Appl. Mater. Interfaces* **2018**, 10, (32), 26972-26981.
- (19) Chen, Y. C.; Ouyang, C. Y.; Song, L. J.; Sun, Z. L., Electrical and Lithium Ion Dynamics in Three Main Components of Solid Electrolyte Interphase from Density Functional Theory Study. *J. Phys. Chem. C* **2011**, 115, (14), 7044-7049.
- (20) Benitez, L.; Seminario, J. M., Ion Diffusivity through the Solid Electrolyte Interphase in Lithium-Ion Batteries. *J. Electrochem. Soc.* **2017**, 164, (11), E3159-E3170.
- (21) Lorget, S.; Usiskin, R.; Maier, J., Transport and Charge Carrier Chemistry in Lithium Oxide. *J. Electrochem. Soc.* **2019**, 166, (10), A2215-A2220.
- (22) Ramasubramanian, A.; Yurkiv, V.; Foroozan, T.; Ragone, M.; Shahbazian-Yassar, R.; Mashayek, F., Lithium Diffusion Mechanism through Solid-Electrolyte Interphase in Rechargeable Lithium Batteries. *J. Phys. Chem. C* **2019**, 123, (16), 10237-10245.
- (23) Peled, E.; Golodnitsky, D.; Ardel, G., Advanced Model for Solid Electrolyte Interphase Electrodes in Liquid and Polymer Electrolytes. *J. Electrochem. Soc.* **1997**, 144, (8), L208-L210.
- (24) Shi, S. Q.; Qi, Y.; Li, H.; Hector, L. G., Defect Thermodynamics and Diffusion Mechanisms in Li<sub>2</sub>CO<sub>3</sub> and Implications for the Solid Electrolyte Interphase in Li-Ion Batteries. *J. Phys. Chem. C* **2013**, 117, (17), 8579-8593.
- (25) Yildirim, H.; Kinaci, A.; Chan, M. K. Y.; Greeley, J. P., First-Principles Analysis of Defect Thermodynamics and Ion Transport in Inorganic SEI Compounds: LiF and NaF. *ACS Appl. Mater. Interfaces* **2015**, 7, (34), 18985-18996.
- (26) Kamphaus, E. P.; Angarita-Gomez, S.; Qin, X. P.; Shao, M. H.; Engelhard, M.; Mueller, K. T.; Murugesan, V.; Balbuena, P. B., Role of Inorganic Surface Layer on Solid Electrolyte Interphase Evolution at Li-Metal Anodes. *ACS Appl. Mater. Interfaces* **2019**, 11, (34), 31467-31476.
- (27) Huggins, R. A., Recent Results on Lithium Ion Conductors. *Electrochim. Acta* **1977**, 22, 773-781.
- (28) Biefeld, R.; Johnson, R., Ionic Conductivity of Li<sub>2</sub>O-Based Mixed Oxides and the Effects of Moisture and LiOH on Their Electrical and Structural Properties. *J. Electrochem. Soc.* **1979**, 126, (1), 1-6.

- (29) Mousa, M.; Oei, Y.; Richtering, H., NMR Investigations of Cation Diffusion in Some Solids with Antifluorite Structure. *J. Phys. Colloq.* **1980**, 41, (C6), C6-223-C6-226.
- (30) Ohno, H.; Konishi, S.; Noda, K.; Takeshita, H.; Yoshida, H.; Watanabe, H.; Matsuo, T., Conductivities of a Sintered Pellet and a Single Crystal of Li<sub>2</sub>O. *J. Nucl. Mater.* **1983**, 118, (2-3), 242-247.
- (31) Chadwick, A.; Flack, K.; Strange, J.; Harding, J., Defect Structures and Ionic Transport in Lithium Oxide. *Solid State Ion.* **1988**, 28, 185-188.
- (32) Indris, S.; Heitjans, P.; Roman, H. E.; Bunde, A., Nanocrystalline Versus Microcrystalline Li<sub>2</sub>O:B<sub>2</sub>O<sub>3</sub> Composites: Anomalous Ionic Conductivities and Percolation Theory. *Phys. Rev. Lett.* **2000**, 84, (13), 2889.
- (33) Churikov, A. V.; Gamayunova, I. M.; Shirokov, A. V., Ionic Processes in Solid-Electrolyte Passivating Films on Lithium. *J. Solid State Electrochem.* **2000**, 4, (4), 216-224.
- (34) Churikov, A. V.; Nimon, E. S.; Lvov, A. L., Impedance of Li-Sn, Li-Cd and Li-Sn-Cd Alloys in Propylene Carbonate Solution. *Electrochim. Acta* **1997**, 42, (2), 179-189.
- (35) He, M.; Guo, R.; Hobold, G. M.; Gao, H.; Gallant, B. M., The Intrinsic Behavior of Lithium Fluoride in Solid Electrolyte Interphases on Lithium. *Proc. Natl. Acad. Sci. U.S.A.* **2020**, 117, (1), 73-79.
- (36) Barr, T. L.; Seal, S., Nature of the Use of Adventitious Carbon as a Binding-Energy Standard. *J. Vac. Sci. Technol. A* **1995**, 13, (3), 1239-1246.
- (37) David, D.; Froning, M.; Wittberg, T.; Moddeman, W., Surface Reactions of Lithium with the Environment. *Appl. Surf. Sci.* **1981**, 7, (3), 185-195.
- (38) Zavadil, K. R.; Armstrong, N. R., Surface Chemistries of Lithium: Detailed Characterization of the Reactions with O<sub>2</sub> and H<sub>2</sub>O Using XPS, EELS, and Microgravimetry. *Surf. Sci.* **1990**, 230, (1-3), 47-60.
- (39) Li, Y. Z.; Li, Y. B.; Sun, Y. M.; Butz, B.; Yan, K.; Koh, A. L.; Zhao, J.; Pei, A.; Cui, Y., Revealing Nanoscale Passivation and Corrosion Mechanisms of Reactive Battery Materials in Gas Environments. *Nano Lett.* **2017**, 17, (8), 5171-5178.
- (40) Wood, K. N.; Teeter, G., XPS on Li-Battery-Related Compounds: Analysis of Inorganic SEI Phases and a Methodology for Charge Correction. *ACS Appl. Energy Mater.* **2018**, 1, (9), 4493-4504.
- (41) Thevenin, J., Passivating Films on Lithium Electrodes - an Approach by Means of Electrode Impedance Spectroscopy. *J. Power Sources* **1985**, 14, (1-3), 45-52.
- (42) Aurbach, D.; Zaban, A.; Gofer, Y.; Abramson, O.; Benzion, M., Studies of Li Anodes in the Electrolyte System 2Me-THF/THF/Me-Furan/LiAsF<sub>6</sub>. *J. Electrochem. Soc.* **1995**, 142, (3), 687-696.
- (43) Moshtev, R.; Puresheva, B., AC Impedance Study of the Lithium Electrode in Propylene Carbonate Solutions: Part I. Effect of the Surface Preparation on the Initial Impedance Parameters. *J. Electroanal. Chem.* **1984**, 180, (1-2), 609-617.
- (44) Zaban, A.; Zinigrad, E.; Aurbach, D., Impedance Spectroscopy of Li Electrodes. 4. A General Simple Model of the Li-Solution Interphase in Polar Aprotic Systems. *J. Phys. Chem.* **1996**, 100, (8), 3089-3101.
- (45) Aurbach, D., Review of Selected Electrode-Solution Interactions Which Determine the Performance of Li and Li Ion Batteries. *J. Power Sources* **2000**, 89, (2), 206-218.
- (46) Andeen, C.; Fontanella, J.; Schuele, D., Low-Frequency Dielectric Constant of LiF, NaF, NaCl, NaBr, KCl, and KBr by the Method of Substitution. *Phys. Rev. B* **1970**, 2, (12), 5068.
- (47) Shi, S. Q.; Lu, P.; Liu, Z. Y.; Qi, Y.; Hector, L. G.; Li, H.; Harris, S. J., Direct Calculation of Li-Ion Transport in the Solid Electrolyte Interphase. *J. Am. Chem. Soc.* **2012**, 134, (37), 15476-15487.
- (48) Pan, J.; Cheng, Y. T.; Qi, Y., General Method to Predict Voltage-Dependent Ionic Conduction in a Solid Electrolyte Coating on Electrodes. *Phys. Rev. B* **2015**, 91, (13).
- (49) Smyth, D. M., *The Defect Chemistry of Metal Oxides*. 2000.
- (50) Jacobs, P. W. M.; Vernon, M. L., Defect Energies for Magnesium Oxide and Lithium Oxide. *J. Chem. Soc., Faraday Trans.* **1990**, 86, (8), 1233-1238.
- (51) Lau, K. C.; Curtiss, L. A.; Greeley, J., Density Functional Investigation of the Thermodynamic Stability of Lithium Oxide Bulk Crystalline Structures as a Function of Oxygen Pressure. *J. Phys. Chem. C* **2011**, 115, (47), 23625-23633.
- (52) Islam, M. M.; Bredow, T.; Minot, C., Theoretical Analysis of Structural, Energetic, Electronic, and Defect Properties of Li<sub>2</sub>O. *J. Phys. Chem. B* **2006**, 110, (19), 9413-9420.
- (53) Li, C. L.; Gu, L.; Maier, J., Enhancement of the Li Conductivity in LiF by Introducing Glass/Crystal Interfaces. *Adv. Funct. Mater.* **2012**, 22, (6), 1145-1149.
- (54) Li, Y. Z.; Huang, W.; Li, Y. B.; Pei, A.; Boyle, D. T.; Cui, Y., Correlating Structure and Function of Battery Interphases at Atomic Resolution Using Cryoelectron Microscopy. *Joule* **2018**, 2, (10), 2167-2177.
- (55) Aurbach, D.; Daroux, M.; McDougall, G.; Yeager, E., Spectroscopic Studies of Lithium in an Ultrahigh Vacuum System. *J. Electroanal. Chem.* **1993**, 358, (1-2), 63-76.
- (56) Kanamura, K.; Tamura, H.; Shiraiishi, S.; Takehara, Z. i., XPS Analysis of Lithium Surfaces Following Immersion in Various Solvents Containing LiBF<sub>4</sub>. *J. Electrochem. Soc.* **1995**, 142, (2), 340-347.